Corrosion Science 236 (2024) 112235

Contents lists available at ScienceDirect

Corrosion Science

journal homepage: www.elsevier.com/locate/corsci

Numerical exploration of a fully mechanistic mathematical model of aqueous CO_2 corrosion in steel pipelines

Michael Jones [a], Joshua Owen [a], Gregory de Boer [a], Richard C. Woollam [a], Mariana C. Folena [b], Hanan Farhat [b], Richard Barker [a,*]

[a] Institute of Functional Surfaces, School of Mechanical Engineering, University of Leeds, Leeds LS2 9JT, United Kingdom
[b] The Corrosion Center of Qatar Environment & Energy Research Institute, Hamad Bin Khalifa University, Doha 34110, Qatar

ARTICLE INFO

Keywords:
CO_2 corrosion
Boundary layer
Mechanistic modelling
Iron carbonate
Simulation

ABSTRACT

A numerical exploration of a comprehensive mechanistic aqueous carbon dioxide (CO_2) corrosion model is conducted across a range of temperatures (273–313 K), CO_2 partial pressures (0.1–1 bar), and bulk pHs (5–6.5). Contour plots are produced to examine the impact on corrosion rate, surface pH, and surface saturation index of iron carbonate ($FeCO_3$). Two response patterns are identified depending upon the limiting behaviour of the system, with a transition from charge-transfer control to mass-transport control as temperature is increased and partial pressure is reduced. $FeCO_3$ surface saturation shows a strong correlation with the release of Fe^{2+} and increase in bulk pH.

1. Introduction

Accurate estimation of corrosion rates is crucial in the design and operation of pipelines and associated infrastructure across the energy sector. Projected corrosion rates directly influence critical design choices such as material selection, as well as informing operational strategies, such as the necessity for corrosion mitigation, inspection, and monitoring. Underestimating corrosion rates can result in failures, posing risks to health, safety, and the environment, as well as substantial financial losses due to production disruptions and equipment replacements. Conversely, overly high estimates can significantly impact the economic viability of a project.

Uniform carbon dioxide (CO_2) corrosion of mild steel can be considered as one of the most studied and well understood corrosion systems, with numerous studies/reviews covering specific aspects of this corrosion system and the underlying physicochemical processes [1,2].

With the increasing interest in oil and gas exploration and production in harsher, more corrosive environments, coupled with the increase in activities in geothermal energy and carbon capture and storage, there remains a strong and growing requirement to create models with increased flexibility to cover a wider spectrum of conditions applicable to new and evolving industrial processes. Mathematical models for CO_2 corrosion prediction developed to date are categorized into three main groups: (i) empirical/semi-empirical models which rely solely on fitting functions to experimental data, (ii) elementary mechanistic models which employ decoupled descriptions of the underlying physicochemical processes, and (iii) comprehensive mechanistic models which employ fully coupled descriptions of the underlying physicochemical processes [1].

Empirical/semi-empirical models were developed predominantly in the 1980s and 1990s, yet continue to be used, largely due to their simplicity and ease of use. However, these models are often limited by a narrow range of applicability. As empirical models are not underpinned by theoretical foundations, they cannot be readily extrapolated beyond the conditions from which they have been experimentally derived. They also offer little insight into the underlying physicochemical changes that occur throughout the corrosion process as the individual interactions are not modelled [1].

These limitations are, at least in part, addressed by the development of comprehensive mechanistic models, which are well rooted in the fundamental physicochemical theory of corrosion processes. Both empirical and mechanistic models have previously been found to accurately predict corrosion rates under acidic conditions up to moderate temperatures. However, mechanistic models have increased flexibility in their application, allowing evaluation of intermediate variables and providing greater clarity on the controlling influences [3]. Yet, it is important to acknowledge that in every case current corrosion models become significantly less accurate once additional factors such as film

---

* Corresponding author.
E-mail address: r.j.barker@leeds.ac.uk (R. Barker).

https://doi.org/10.1016/j.corsci.2024.112235
Received 7 May 2024; Received in revised form 12 June 2024; Accepted 24 June 2024
Available online 26 June 2024
0010-938X/© 2024 The Author(s). Published by Elsevier Ltd. This is an open access article under the CC BY license (http://creativecommons.org/licenses/by/4.0/).

formation or oil wetting are introduced [4,5].

Overall, comprehensive mechanistic models provide the greatest insight into the corrosion process, as well as facilitating the inclusion of additional physical phenomena. Regrettably, the downsides of such models are that they are complex, computationally more intensive, and are often built in such a way as to be unfavourable to the production of large data sets. As a result, they are often only utilised to perform detailed analysis for a select set of conditions and cannot be used effectively to assess the entire range of conditions seen within many industrial applications.

In recognition of this limitation, this paper outlines the process of building a comprehensive mechanistic CO_2 corrosion model within COMSOL Multiphysics® based on the work of Kahyarian and Nešić[6,7], whereby the state-of-art in the context of comprehensive CO_2 corrosion modelling is outlined. After describing the construction of the model, a numerical exploration of its outputs is performed, generated via the use of parametric sweeps, to evaluate the model performance, identify key trends in the predicted responses, and to improve the overall understanding of the underlying interactions controlling the CO_2 corrosion process.

2. CO_2 corrosion mechanism and the structure/evolution of CO_2 corrosion models

Prior to the creation of the CO_2 corrosion model in COMSOL Multiphysics®, it is perhaps prudent to describe the CO_2 corrosion mechanism for completeness, followed by outlining the basic principles, structure, and approach for modelling electrochemical systems, as well as describe the extent to which comprehensive mechanistic models have evolved over the past few decades.

2.1. Bulk equilibrium reactions

Uniform corrosion of a steel surface, such as the internal surface of a pipeline, occurs in the presence of dissolved CO_2 due to a series of reactions that occur both in the fluid and at the surface. When CO_2 is dissolved in water, a slow hydration reaction occurs to produce carbonic acid (H_2CO_3):

$$CO_{2_{(aq)}} + H_2O_{(l)} \rightleftharpoons H_2CO_{3_{(aq)}} \tag{1}$$

Following the hydration reaction, two dissociation reactions take place, resulting in the production of hydrogen (H^+) ions at each stage:

$$H_2CO_{3_{(aq)}} \rightleftharpoons HCO^-_{3_{(aq)}} + H^+_{(aq)} \tag{2}$$

$$HCO^-_{3_{(aq)}} \rightleftharpoons CO^{2-}_{3_{(aq)}} + H^+_{(aq)} \tag{3}$$

Additionally, the dissociation of the water itself contributes to the production of ions in solution:

$$H_2O_{(l)} \rightleftharpoons H^+_{(aq)} + OH^-_{(aq)} \tag{4}$$

When the pH is high, hydroxylation reactions (Eqs. 5 and 6) act to reduce the hydroxide ion concentration. Under acidic conditions however, the contribution of these reactions is negligible [6].

$$CO_{2_{(aq)}} + OH^-_{(aq)} \rightleftharpoons HCO^-_{3_{(aq)}} \tag{5}$$

$$HCO^-_{3_{(aq)}} + OH^-_{(aq)} \rightleftharpoons CO^{2-}_{3_{(aq)}} + H_2O_{(l)} \tag{6}$$

2.2. Surface reactions

The corrosion observed on the steel surface is due to the anodic dissolution of iron (Fe) (Eq. 7) which is driven by the presence hydrogen ions which reduce in the cathodic reaction to form hydrogen gas (Eq. 8):

$$Fe_{(s)} \rightarrow Fe^{2+}_{(aq)} + 2e^- \tag{7}$$

$$2H^+_{(aq)} + 2e^- \rightarrow H_{2_{(g)}} \tag{8}$$

An early direct reduction model proposed by De Waard and Milliams [8] suggested an additional cathodic reaction in the form of direct reduction of carbonic acid. However, in recent years it has been proposed that the carbonic acid instead acts as a buffer at the interface, dissociating to rapidly replenish hydrogen ions as they are consumed [9–11]. Due to the difficulties associated with isolating these surface reactions [1], the specific mechanisms are still debated. However, for the purposes of this work, hydrogen reduction is assumed to be the sole cathodic surface reaction, in alignment with the most recent published models [6,7,10,12].

2.3. Transportation of species

There are three mechanisms by which charged species can be transported within a fluid: diffusion, electromigration, and convection. To accurately model CO_2 corrosion it is important that each of these modes of species transport are considered. These three terms are commonly combined in a single equation to calculate the flux of species:

$$N_j = -D_{M,j}\frac{\partial c_j}{\partial x} - z_j u_j F c_j \frac{\partial \Phi}{\partial x} + c_j v \tag{9}$$

Where N_j is the flux of species j ($mol{\cdot}m^{-2}{\cdot}s^{-1}$), $D_{M,j}$ is the molecular diffusion coefficient ($m^2{\cdot}s^{-1}$), c_j is the concentration ($mol{\cdot}m^{-3}$), x is the distance perpendicular to the surface (m), z_j is the valence, u_j is the mobility of species ($mol{\cdot}s{\cdot}kg^{-1}$), F is the Faraday constant ($C{\cdot}mol^{-1}$), Φ is the electrolyte potential (V), and v is the solution velocity ($m{\cdot}s^{-1}$).

The conservation of mass principle is then applied to calculate the transport of species via the Nernst-Planck equation, given by Eq. 10 for a one-dimensional model. The Nernst-Planck equation accounts the species flux as well as the production/consumption of species via the electrochemical surface reactions and boundary layer kinetic reactions discussed later.

$$\frac{\partial c_j}{\partial t} = -\frac{\partial N_j}{\partial x} + R_j \tag{10}$$

Where R_j is a source/sink term describing the local change in species j ($mol{\cdot}m^{-3}{\cdot}s^{-1}$).

As demonstrated by Thorat et al. [13] and Owen et al. [14], it is possible to fully model the transportation of species using Computational Fluid Dynamics (CFD). However, for simplicity it is common to utilise empirically derived equations such as those proposed by Davies [15] and Aravinth [16]. In some instances, it is the case that simplifications can be made to the transport equation to reduce complexity whilst still accounting for the movement of ions. For example, if the fluid is static with no external stirring, then the solution velocity (v) becomes zero and the convection term is also zero ($c_j v = 0$). Similarly, if there is a sufficiently large concentration of an inert electrolyte present within the solution, the electric potential gradient becomes small enough to consider the electromigration term negligible ($z_j u_j F c_j \frac{\partial \Phi}{\partial x} \approx 0$) [17,18].

2.4. Basic principles and evolution of comprehensive mechanistic CO_2 corrosion models since the 1990s

An introduction to the basic principles of modelling electrochemical systems are detailed in a 2019 paper by Stephens and Mauzeroll [17]. In general, the models function by dividing a one-dimensional domain into the corroding surface, the bulk solution, and the boundary layer between them. Mathematical equations are subsequently assigned to each section, describing local reactions and concentration changes which are then combined with a global transport equation to describe how species move through the boundary layer. A more comprehensive overview of these electrochemical modelling methods is provided by Britz and Strutwolf [18].

In terms of predictive model evolution in 1992, Turgoose et al. [19] developed the first comprehensive mechanistic model for CO_2 corrosion. In this early model, existing understanding of the bulk chemistry and corrosive mechanisms were combined using a finite element model to predict corrosion rates and boundary layer speciation for a rotating disk electrode. Although the model formed a solid starting point for future work, it assumed complete consumption of H_2CO_3 and H^+ at the surface and was therefore only valid under mass-transfer limited conditions. Additionally, the model did not account for the migratory effects of charge separation, the 2nd term in the flux equation (Eq. 9), nor did it accurately account for the convective term in the near-wall region. These issues were, however, addressed in a subsequent model produced by Nordsveen et al. [20,21].

The Nordsveen et al. [21] model utilised a modified version of the species flux equation (Eq. 9) to predict the movement of species through the boundary layer. For continuum hydrodynamic models, the velocity of a fluid is taken as zero at the surface [22], however, turbulent eddies may still permeate through the boundary layer making it difficult to accurately model the instantaneous velocity in the near-wall region. The convection term ($c_j v$) was therefore instead approximated via a turbulent diffusivity (D_T) term, as proposed by Davies [15], to capture the effect of turbulent eddies and their dissipation closer to the surface. As well as unifying and simplifying the transport terms, the model also implemented an expression for the charge transfer rate by way of the Tafel equation. The use of the Nernst-Planck equation (Eq. 10) alongside the Tafel equation allows for the calculation of the exchange current density from the local surface concentrations of all electroactive species, expanding the applicability of the model past mass-transfer limiting conditions.

However the model by Nordsveen et al. [21] did not include calculations of activity coefficients in the equilibrium calculations, which may lead to inaccuracy at higher ionic strengths ($I > 0.01M$) [23]. Additionally, they included direct reduction of carbonic acid at the surface, originally proposed by De Waard and Milliams[8], as a secondary cathodic reaction which has since been disputed in the literature [1,9–11]. Despite this, the model provided a solid model framework that has been employed in subsequent comprehensive mechanistic models, such as the models by Song et al. [24], Remita et al. [9] and, more recently, Kahyarian and Nešić [6,7].

The 2003 paper by Nordsveen *et al* [21]. formed the first in a series of three papers based around this corrosion model, with subsequent papers by Nešić *et al*[25]. and Nešić and Lee[26]. These additional works highlight the benefit of a comprehensive mechanistic CO_2 corrosion model by utilising the predicted surface speciation to model the formation of protective iron carbonate ($FeCO_3$) films. It was shown that bulk pH, temperature, CO_2 partial pressure, dissolved iron concentration, and fluid velocity are all highly influential factors in the formation of $FeCO_3$ films, whilst also demonstrating the importance of understanding surface chemistry in these predictions due to the noticeable divergence from the bulk properties.

In 2019, Kahyarian et al. [7] produced a new comprehensive mechanistic model that introduced a number of updates to the earlier work by Nordsveen et al. [20,21]. The most significant change was the removal of the direct carbonic acid reduction reaction, utilising the proposed buffering mechanism to describe the surface behaviour with the only cathodic reaction being hydrogen reduction. However, there were further changes made to the equilibrium and rate constants, the hydrodynamic inputs, as well as the anodic mechanisms. A year later, an updated version of the model was published [6] providing additional insights into the model as well as including the effect of activity

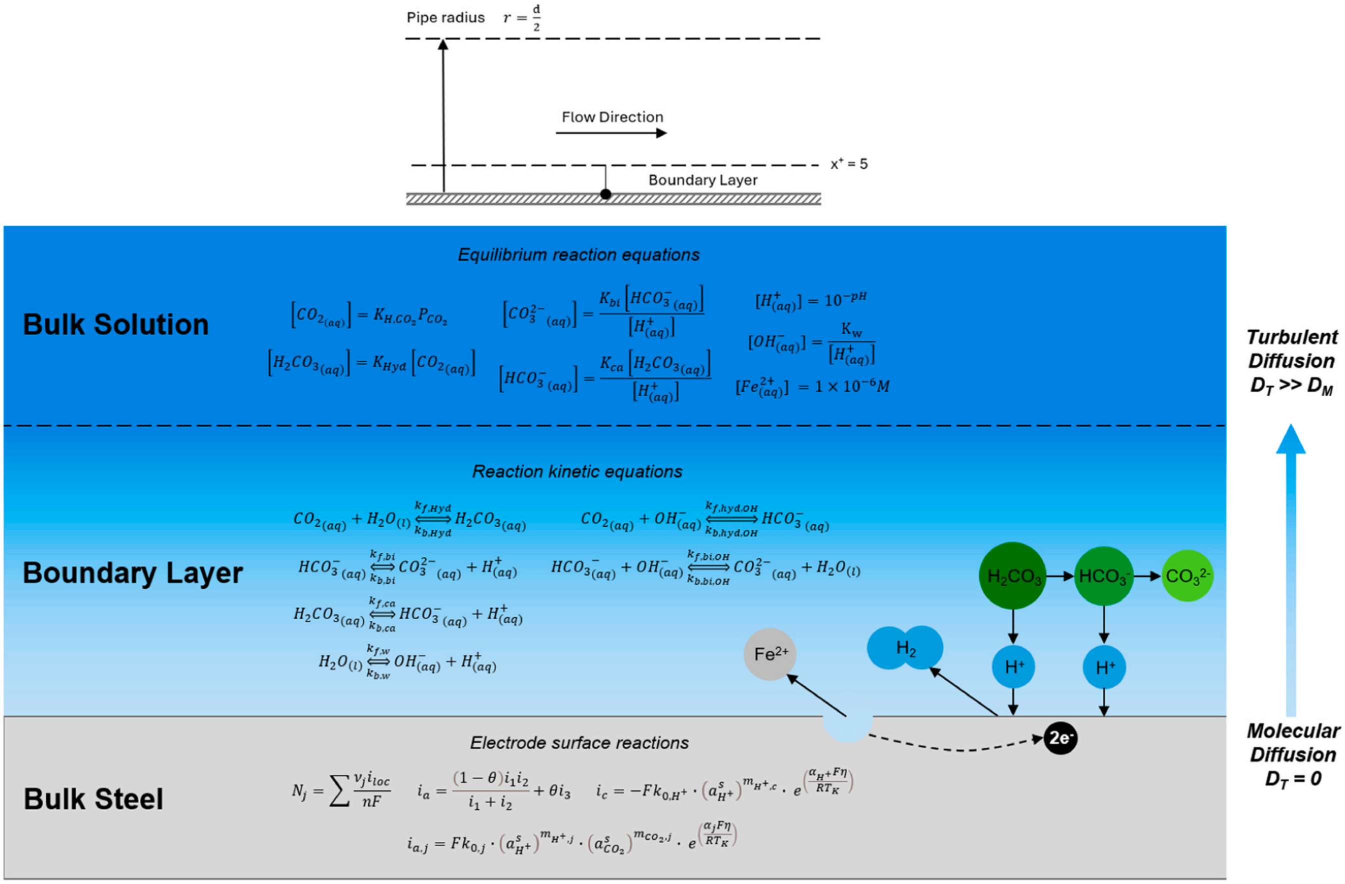

Fig. 1. Diagram showing the system being modelled within system, represented mathematically by a one-dimensional line between the steel surface and the bulk solution.

coefficients. Building on this work, in 2022 Alsalem et al. [12] followed a similar approach to predict corrosion across the surface of a rotating cylinder electrode (RCE). As with the earlier model by Nordsveen et al. [21], Alsalem et al. [12] advanced the corrosion model further by incorporating precipitation of $FeCO_3$ via the surface species concentrations. The model was validated against experimental data from an RCE and therefore included some analysis of the influence of hydrodynamics on the corrosion behaviour, examining how the changes in the tangential surface velocity affected the corrosion rate as well as the coverage and thickness of the $FeCO_3$ layer.

3. Overview of corrosion model and underlying physics

Before describing the process of creating of the CO_2 corrosion model within COMSOL, it is important to properly define the scenario that is being modelled. The model is a one-dimensional representation of the interaction between aqueous CO_2 and the internal surface of a mild steel pipeline. The model evaluates corrosion and speciation outwards from a single point on the steel surface which can be split into three key domains: bulk steel surface, boundary layer, and bulk solution. These can be modelled as a straight line representing the boundary layer, with the two endpoints being representative of the corroding bulk steel surface and the bulk fluid, respectively. The behaviour of the active species in each of these domains is described by different sets of equations to model the production, consumption, and transport of the species. A two-dimensional visualization of the system can be seen in Fig. 1, including complete sets of equations describing each of the three domains.

Uniform corrosion is assumed in the model when calculating corrosion rates, along with zero precipitation of solid corrosion product either within the boundary or at the metal surface (coupled film formation is difficult to model accurately due to the complexity of precipitation kinetics [27,28], however the 'scaling tendency' as proposed by Van Hunnik et al. [29] can be calculated to predict when protective films will begin to form). Empirical relationships are used to calculate the thickness of the boundary layer and effect of turbulence, based on data for a fully developed straight pipe flow. These relationships assume flow is uniform throughout the pipe and axisymmetric about the centre.

3.1. Fluid properties

For the model, standard values were selected for the fluid properties representative of CO_2 saturated water flowing through a straight pipe under turbulent hydrodynamic conditions. The properties of the fluid were calculated based upon variable inputs, which are shown in Table 1 alongside the range of values selected in this work.

A summary of the hydrodynamic input parameters is shown in Table 2 alongside calculated values for a temperature of 293.15 K and a partial pressure of CO_2 of 1 bar.

Table 1
Summary of input variables and the associated range of values used.

Variable	Symbol	Range of Values	Number of Points	Interval
Temperature (K)	T_K	273.15 – 313.15 K	41	1 K
Partial Pressure of CO_2	P_{CO_2}	0.1 – 10 bar	161	80 points/decade
pH	pH	5 – 6.5	4	0.5
Bulk Fluid Velocity	v	1 – 10 m·s^{-1}	19	0.5

3.2. Geometry and discretization

To represent the geometry within the COMSOL model, an interval between two points was used. These points represented the metal surface and the bulk-boundary interface respectively, with x-coordinate limits of zero and δ respectively, where δ denotes the boundary layer thickness. Linearly distributed edge elements with a maximum element size of 10^{-7} m were used to generate a uniformly dense mesh, ensuring accurate resolution of concentration gradients for boundary layers as small as 10 µm.

To determine the value of δ and hence the size of the domain, it is necessary to understand the interaction between the fluid and the surface. In near-wall environments, it has been previously demonstrated that the relative fluid velocity tends to zero at the surface, this is known as the 'no-slip condition' for continuum hydrodynamics [22,30]. For fluid flow within a straight pipe, the influence of the no-slip condition can be described by universal law of the wall [31]. It is possible to use this relationship to define the boundary layer thickness (the height of the laminar region closest the wall) as a function of the dimensionless wall distance (x^+). The transition from the laminar (viscous) sublayer to the buffer layer occurs when $x^+ = 5$ [30]. The height of the boundary layer (δ) can therefore be defined as the perpendicular distance from the surface (x) at this point.

$$x^+ = \frac{x\left(\frac{\tau_\omega}{\rho}\right)^{\frac{1}{2}}}{\nu} \tag{14}$$

Given that $x = \delta$ when $x^+ = 5$, these values can be substituted into Eq. 14 to give:

$$\delta = \frac{5\nu}{\left(\frac{\tau_\omega}{\rho}\right)^{\frac{1}{2}}} \tag{15}$$

Where τ_ω is the wall shear stress (Pa), which can be found as a function of the Fanning friction factor (C_f) at the wall, calculated using the correlation provided by Swamee and Jain [32].

$$\tau_\omega = \frac{\rho C_f u^2}{2} \tag{16}$$

$$C_f = \frac{C_d}{4} = \frac{1}{16\left(\log\left(\frac{\varepsilon}{3.7d} + \frac{5.74}{Re^{0.9}}\right)\right)^2} \tag{17}$$

Where C_d is the Darcy friction factor, ε is the surface roughness (m) (assumed to be negligible, $\varepsilon \approx 0$), and d is the pipe diameter (m).

Due to the very low flow velocities within the boundary layer, mass transport due to convection becomes very small within this region. However, turbulent eddies still permeate through the boundary and

Table 2
Summary of formulae used in the calculation of the hydrodynamic properties and calculated values for a temperature (T) of 293.15 K and 1 bar P_{CO2}.

Parameter	Symbol	Formula [6]	Value (SI Units)	Equation
Density of Fluid	ρ_f	$(753.596 + 1.87748T_K - 0.003564T_K^2)$	997.7 kg·m^{-3}	(11)
Hydraulic Diameter	d	-	0.1m	-
Dynamic Viscosity	μ	$0.001002 \times 10^{\left(\frac{1.1709(293.15 - T_K) - 0.001827(293.15 - T_K)^2}{(T_K - 273.15) + 89.93}\right)}$	0.0010015 kg·m^{-1}·s^{-1}	(12)
Reynolds Number	Re	$\frac{\rho_f v d}{\mu}$	99619	(13)

influence the rate of species transport near the surface [15]. In order to account for this effect, the flux equation (Eq. 9) is modified to remove the convection term and instead incorporate a turbulent diffusivity (D_T) value (Eq. 18).

$$N_j = -(D_{Mj} + D_T)\frac{\partial c_j}{\partial x} - z_j u_j F c_j \frac{\partial \Phi}{\partial x} \tag{18}$$

Turbulent diffusivity can be calculated as a function of x^+, as discussed by Notter and Sleicher [33]. In this work, the expression provided by Aravinth [16] is used, utilising the form of the Notter and Sleicher [33] equation with more recent values from Churchill [34].

$$D_T = \frac{0.0007(x^+)^3}{\sqrt{\left(1 + 0.00405(x^+)^2\right)}} \tag{19}$$

3.3. Active species

A total of nine species are included within the speciation calculations, seven of which are the active species within Eqs. 1–8 (excluding H_2O). Additional species Na^+ and Cl^- are included as ions to balance the charge when the bulk pH is specified and shifted from the equilibrium pH. Each individual species' associated coefficients relating to its chemical activity, and diffusion coefficient are provided in Table 3.

The reference diffusion coefficient given in Table 3 represents the diffusion coefficient at a temperature of 293.15 K. The temperature dependence of the diffusion coefficient is then estimated by the Stokes-Einstein equation:

$$D_i = D_{i,ref}\left(\frac{T_K}{T_{ref}}\right)\left(\frac{\mu_{ref}}{\mu}\right) \tag{20}$$

Where T_{ref} is the reference temperature (293.15 K) and μ_{ref} is the reference viscosity (0.001002 $kg\cdot m^{-1}\cdot s^{-1}$).

The non-ideal behaviour of the chemical species is described by the associated activity coefficient, which is often assumed to be equal to one for dilute solutions[7,9,20,21,24]. However, in this work, an approximation for each species' activity coefficient is used to provide a more realistic representation of the ionic behaviour. The extended form of the Debye-Hückel equation (Eq. 21) is implemented, using the charge values and ion radii stated in Table 3.

$$\ln(\gamma_i) = -\frac{A z_i^2 \sqrt{I}}{1 + B a_i \sqrt{I}} \tag{21}$$

Where A and B are characteristic constants of the fluid and I is the ionic strength of the solution (M).

$$A = \frac{F^2 \epsilon_0 \sqrt{2}}{8\pi(\epsilon R T_K)^{\frac{3}{2}}} \tag{22}$$

Table 3
Summary of active species with associated charge, ion size and reference diffusion coefficient.

Species	Diffusion Coefficient ($D_{i,ref}$) [6]	Charge (z_i)	Ionic Radius (a_i, nm) [23]
$CO_{2\,(aq)}$	1.92×10^{-9}	0	N/A
$H_2CO_{3\,(aq)}$	1.75×10^{-9}	0	N/A
$HCO_3^-(aq)$	1.185×10^{-9}	-1	0.45
$CO_3^{2-}(aq)$	0.923×10^{-9}	-2	0.45
$H^+_{(aq)}$	9.315×10^{-9}	$+1$	0.9
$OH^-_{(aq)}$	5.273×10^{-9}	-1	0.35
$Fe^{2+}_{(aq)}$	0.72×10^{-9}	$+2$	0.6
$Na^+_{(aq)}$	1.334×10^{-9}	$+1$	0.45
$Cl^-_{(aq)}$	2.032×10^{-9}	-1	0.3

$$B = \frac{F}{\sqrt{\frac{\epsilon R T_K}{2}}} \tag{23}$$

Where F is the Faraday constant (96,458 $C\cdot mol^{-1}$), ϵ_0 is the permittivity of free space, ϵ is the relative permittivity of the solution (80 for water at 1 bar, 293.15 K)[35], and R is the universal gas constant (8.3145 $J\cdot mol^{-1}\cdot K^{-1}$).

For a solution of 1 wt% sodium chloride (NaCl) solution the ionic strength is 0.1711 M, given by:

$$I = \frac{1}{2}\sum_{j=1}^{n} c_j z_j^2 \tag{24}$$

3.4. Bulk fluid chemistry

For a given set of conditions, each species within the CO_2/H_2O system will reach a stable equilibrium concentration in the bulk solution, forming a boundary condition for the model. As can be seen from the reactions shown in Eqs. 1–4, each reaction in the solution occurs simultaneously forwards and backwards. For an isothermal system, these reactions reach a steady state and the concentrations of each species remain constant. The composition of the bulk fluid can be calculated via equilibrium constants (defined by Eqs. 25–31).

$$H_{CO_2} = \frac{P_{CO_2}}{a_{CO_2\,(aq)}} \tag{25}$$

$$K_{Hyd} = \frac{a_{H_2CO_3\,(aq)}}{a_{CO_2\,(aq)} \cdot a_{H_2O_{(l)}}} \tag{26}$$

$$K_{ca} = \frac{a_{HCO_3^-\,(aq)} \cdot a_{H^+\,(\mathrm{aq})}}{a_{H_2CO_3\,(aq)}} \tag{27}$$

$$K_{bi} = \frac{a_{CO_3^{2-}\,(aq)} \cdot a_H^+(aq)}{a_{HCO_3^-\,(aq)}} \tag{28}$$

$$K_W = \frac{a_{OH^-\,(aq)} \cdot a_{H^+\,(aq)}}{a_{H_2O\,(l)}} \tag{29}$$

$$K_{ca} \cdot \frac{K_{Hyd}}{K_W} = \frac{a_{HCO_3^-\,(aq)}}{a_{CO_2\,(aq)} \cdot a_{OH^-\,(aq)}} \tag{30}$$

$$\frac{K_{bi}}{K_W} = \frac{a_{CO_3^{2-}\,(\mathrm{aq})} \cdot a_{H_2O\,(l)}}{a_{HCO_3^-\,(aq)} \cdot a_{OH^-\,(aq)}} \tag{31}$$

The values used to calculate the equilibrium constants are shown in Table 4, with the associated formulae shown in Eqs. 32–34. Note that some of these values differ from the values reported by Kahyarian and Nešić [6] due to minor differences relative to the original works. All values reported here reflect those in the source literature.

$$\ln\left(H^*_{CO_{2^*}}\right) = a_1 + a_2 T_K + \frac{a_3}{T_K} + \frac{a_4}{T_K^2} \tag{32}$$

$$\log(K_w) = a_1 + \frac{a_2}{T_K} + \frac{a_3}{T_K^2} + \frac{a_4}{T_K^3} + \left(a_5 + \frac{a_6}{T_K} + \frac{a_7}{T_K^2}\right)\log\left(\frac{\rho_w}{1000}\right) \tag{33}$$

$$K_{Hyd} = a_1 e \frac{a_2}{R T_K} \tag{34}$$

For K^*_{ca} and K_{bi}:

Table 4
Parameters for the calculation of equilibrium constants.

	$H^{*}_{CO_2}$ [36]	K_{Hyd} [6]	K^{*}_{ca} [37]	K_{bi} [37]	K_w [38]
a_1	1.4000×10^{1}	6.6330×10^{-2}	2.3352×10^{2}	-1.5118×10^{2}	-4.0980
a_2	-1.3341×10^{-2}	9.5260×10^{3}	0.0000	-8.8696×10^{-2}	-3.2452×10^{3}
a_3	-5.5898×10^{2}		-1.1974×10^{4}	-1.3623×10^{3}	2.2362×10^{5}
a_4	-4.2258×10^{5}		0.0000	0.0000	-3.9840×10^{7}
a_5			-3.6506×10^{1}	2.7798×10^{1}	1.3957×10^{1}
a_6			-4.5080×10^{1}	-2.9514×10^{1}	-1.2623×10^{3}
a_7			2.1313×10^{3}	1.3890×10^{3}	8.5641×10^{5}
a_8			6.7143	4.4196	
a_9			8.3939×10^{-3}	3.2200×10^{-3}	
a_{10}			-4.0154×10^{-1}	-1.6445×10^{-1}	
a_{11}			-1.2402×10^{-3}	-4.7367×10^{-4}	

$$\ln(par.) = a_1 + a_2 T_K + \frac{a_3}{T_K} + \frac{a_4}{T_K^2} + a_5 \ln(T_K) + \left(\frac{a_6}{T_K} + \frac{a_7}{T_K^2} + \frac{a_8}{T_K}\ln(T_K)\right)(p - p_s) + \left(\frac{a_9}{T_K} + \frac{a_{10}}{T_K^2} + \frac{a_{11}}{T_K}\ln(T_K)\right)(p - p_s)^2 \tag{35}$$

It should be noted that the calculated values $H^{*}_{CO_2}$ and K^{*}_{ca}, are defined in relation to the total dissolved carbon dioxide (CO_2^{*}) which includes both dissolved CO_2 and hydrated dissolved CO_2 in the form of H_2CO_3. Adjusting these values to give the true dissociation constants, requires some mathematical manipulation. From Eq. 26, assuming the activity of water to be equal to 1, it can be seen that:

$$a_{H_2CO_3} = a_{CO_2} \cdot K_{Hyd} \tag{36}$$

Hence:

$$H^{*}_{CO_2} = \frac{P_{CO_2}}{a^{*}_{CO_2}} = \frac{P_{CO_2}}{\left(a_{CO_2} + a_{H_2CO_3}\right)} = \frac{P_{CO_2}}{a_{CO_2}\left(1 + K_{Hyd}\right)} = \frac{P_{CO_2}}{a_{CO_2}} \cdot \frac{1}{\left(1 + K_{Hyd}\right)} = \frac{H_{CO_2}}{\left(1 + K_{Hyd}\right)}$$

$$H_{CO_2} = H^{*}_{CO_2} \cdot \left(1 + K_{Hyd}\right) \tag{37}$$

For the calculation of K_{ca}:

$$K^{*}_{ca} = \frac{a_{HCO_3^-} \cdot a_{H^+}}{a^{*}_{CO_2}} = \frac{a_{HCO_3^-} \cdot a_{H^+}}{\left(a_{CO_2} + a_{H_2CO_3}\right)} \tag{38}$$

Combining Eqs. 37 and 38:

$$K^{*}_{ca} = \frac{a_{HCO_3^-} \cdot a_{H^+}}{\left(\frac{a_{H_2CO_3}}{K_{Hyd}} + a_{H_2CO_3}\right)} = \frac{a_{HCO_3^-} \cdot a_{H^+}}{a_{H_2CO_3}\left(1 + \frac{1}{K_{Hyd}}\right)} = \frac{a_{HCO_3^-} \cdot a_{H^+}}{a_{H_2CO_3}} \cdot \frac{1}{\left(1 + \frac{1}{K_{Hyd}}\right)} = \frac{K_{ca}}{\left(1 + \frac{1}{K_{Hyd}}\right)}$$

$$K_{ca} = K^{*}_{ca} \cdot \left(1 + \frac{1}{K_{Hyd}}\right) \tag{39}$$

The resulting species concentrations for the bulk fluid over a range of pH values are shown in Fig. 2 for a temperature of 293.15 K, CO_2 partial pressure of 1 bar and ionic strength of 0.1711 M (1 wt% NaCl). It should be noted that a nominal concentration of 1 ppm_{Molar} is given for the concentration of Fe^{2+}, despite not being involved in any reactions in the bulk. This is to account for the accumulation of Fe^{2+} in the bulk resulting from the surface reactions in the system, which cannot be calculated for a stand-alone one-dimensional model. As Fe^{2+} is being released from the surface, the bulk concentration cannot be zero as this would imply zero flux across the boundary.

As the pH of the solution increases, there are relative increases in both dissociated forms of dissolved CO_2, namely HCO_3^- and CO_3^{2-} (Fig. 2). Fig. 3 shows how the ratios of these species change as a function of bulk pH, with undissociated aqueous CO_2 being the dominant form at low pH. At a pH of around 6, this shifts towards a bicarbonate (HCO_3^-) dominated solution, before transitioning again to a carbonate (CO_3^{2-}) dominated solution at around pH 9.

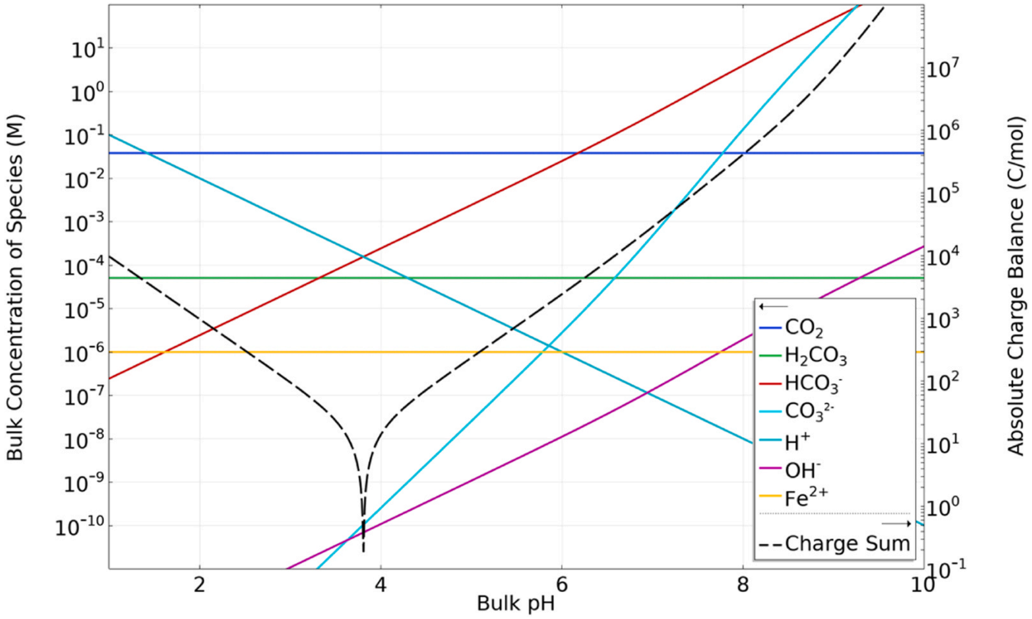

Fig. 2. Bulk species concentration and total charge balance as a function of pH for input values of 20°C, 1 bar P_{CO2} and ionic strength of 0.1711 M.

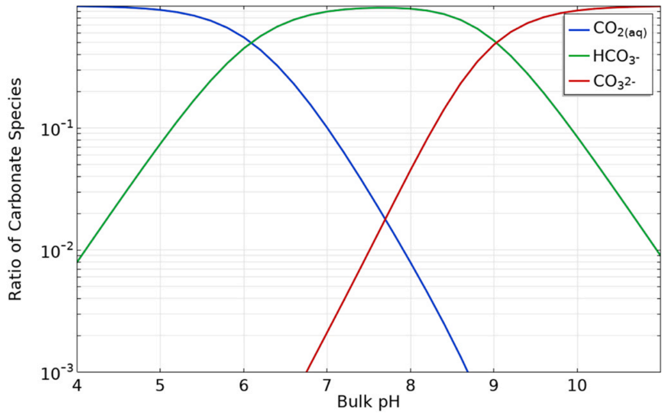

Fig. 3. Ratio of bulk carbonate species as a function of bulk pH.

3.5. *Electrochemical surface reactions*

At the interface between the fluid and the metal surface, electrochemical reactions occur resulting in corrosion of the surface due to the dissolution of solid Fe. Two electrode half-reactions are specified within this model: the anodic dissolution of Fe (Eq. 7) and the cathodic reduction of H^+ (Eq. 8). To calculate a corrosion rate from these reactions within COMSOL a dissolving-depositing species must be specified to represent the surface material. Material properties representative of mild steel were used, specifically the density (ρ_s) and the molar mass (M_w), these values are shown in Table 5.

These two material properties are necessary to determine corrosion rate of the electrode based upon the reaction rate of the dissolving material, which in this case is Fe within the steel. The formulae used to calculate the mass and thickness change at the surface are:

$$\Delta S = M_w N_{Fe} \tag{40}$$

$$CR = \frac{\Delta S}{\rho_s} \tag{41}$$

Where ΔS is mass reaction rate at the surface ($kg{\cdot}m^{-2}{\cdot}s^{-1}$), M_w is the molar mass ($kg{\cdot}mol^{-1}$), N_{Fe} is the molar flux of Fe from the surface ($mol{\cdot}m^{-2}{\cdot}s^{-1}$), and CR is the corrosion rate at the surface ($m{\cdot}s^{-1}$).

The rate of reaction of the dissolving Fe requires the specification of both the cathodic dissolution reaction and the anodic surface reactions. Each of the reactions can be expressed by the general electrochemical reaction formula to determine the stoichiometric coefficients:

$$\sum_{ox} \nu_{ox} S_{ox} + ne^- \leftrightarrow \sum_{red} \nu_{red} S_{red} \tag{42}$$

Where ν is the stoichiometric coefficient, S is the species, and n is the number of participating electrons. Subscript *red* and *ox* indicate products and reactants respectively in a reduction reaction [40].

The stoichiometric coefficients of the anodic dissolution reaction and cathodic reduction reaction are provided in Table 6. Note that ν_{Fe} in Table 6 refers the stoichiometric coefficient of aqueous Fe^{2+} and not solid Fe at the surface.

According to Faraday's laws, the molar species fluxes perpendicular to the surface can be calculated as the sum of all the flux contributions from the electrode reactions (Eq. 43)[40].

Table 5
Material properties of mild steel, representing the dissolving species at the electrode surface.

Material Property	Symbol	Value [39]
Density	ρ_s	$7,850\ kg{\cdot}m^{-3}$
Molar Mass	M_w	$55.845\ g{\cdot}mol^{-1}$

Table 6
Participating electrons and stoichiometric coefficient values for iron oxidation (anodic) and hydrogen evolution (cathodic) surface reactions.

Coefficient	$Fe_{(s)} \rightarrow Fe^{2+}_{(aq)} + 2e^-$	$2H^+_{(aq)} + 2e^- \rightarrow H_{2(g)}$
n	2	2
ν_H	0	− 2
ν_{Fe}	− 1	0

$$N_j = \sum \frac{\nu_j i_{loc}}{nF} \tag{43}$$

Where ν_j is the stoichiometric coefficient of species j, i_{loc} is the local current density ($A{\cdot}m^{-2}$), n is the number of participating electrons, and F is the Faraday constant.

The local current density for the cathodic reaction is calculated from the surface activity of H^+ via Eq. 44.

$$i_c = -Fk_{H^+} \cdot \left(a^s_{H^+}\right)^{m_{H^+,c}} \cdot e^{\left(\frac{\alpha_{H^+} F\eta}{RT_K}\right)} \tag{44}$$

Where k_{H^+} is provided by Eq. 51, $m_{H^+,c}$ and α_{H^+} are constants provided in Table 7, $a^s_{H^+}$ is the surface activity of H^+ ($mol{\cdot}m^{-3}$), and η is the overpotential (V).

The local current density for the anodic reaction is calculated as a function of three current steps ($i_{a,n}$), any of which can be rate determining depending on surface conditions, as discussed by Kahyarian et al. [7]. Each step is a function of the surface activities of both H^+ and aqueous CO_2. An intermediary function, θ is used to describe the transition between three currents as shown by Eqs. 45–47.

$$i_{a,j} = Fk_j \cdot \left(a^s_{H^+}\right)^{m_{H^+,j}} \cdot \left(a^s_{CO_2}\right)^{m_{CO_2,j}} \cdot e^{\left(\frac{\alpha_j F\eta}{RT_K}\right)} \tag{45}$$

$$\theta = \frac{K_\theta \cdot \left(a^s_{H^+}\right)^{m_{H^+,\theta}} \cdot \left(a^s_{CO_2}\right)^{m_{CO_2,\theta}} \cdot e^{\left(\frac{\alpha_\theta F\eta}{RT_K}\right)}}{1 + K_\theta \cdot \left(a^s_{H^+}\right)^{m_{H^+,\theta}} \cdot \left(a^s_{CO_2}\right)^{m_{CO_2,\theta}} \cdot e^{\left(\frac{\alpha_\theta F\eta}{RT_K}\right)}} \tag{46}$$

$$i_a = \frac{(1-\theta) i_{a,1} i_{a,2}}{i_{a,1} + i_{a,2}} + \theta i_{a,3} \tag{47}$$

Where the values of k_j are calculated via Eq. 51, $a^s_{H^+}$ is the surface activity of H^+ in $mol{\cdot}m^{-3}$, $a^s_{CO_2}$ is the surface activity of CO_2 (M), T_K is the temperature (K), η is the overpotential (V) and all other values are constants. The values of these constants are summarised in Table 7.

In each case, the overpotential (η) is given by:

$$\eta = E - E_{rev} \tag{48}$$

Where E is the electric potential (V) and E_{rev} is the reversible potential (V). The electric potential is defined within COMSOL as the difference between the electrode potential (Φ_s) and the electrolyte potential (Φ_l) at

Table 7
Summary of constants used in the calculation of both the cathodic and anodic current density calculations [6].

k_{0,H^+}	$2 \times 10^{-8}\ mol{\cdot}m^{-2}{\cdot}s^{-1}$	$m_{H^+,c}$	0.5	α_{H^+}	0.43
$k_{0,1}$	$4 \times 10^{9}\ mol{\cdot}m^{-2}{\cdot}s^{-1}$	$m_{H^+,1}$	− 2.5	α_1	2.5
$k_{0,2}$	$1 \times 10^{13}\ mol{\cdot}m^{-2}{\cdot}s^{-1}$	$m_{H^+,2}$	1	α_2	2
$k_{0,3}$	$0.8 \times 10^{-3}\ mol{\cdot}m^{-2}{\cdot}s^{-1}$	$m_{H^+,3}$	− 0.5	α_3	0.5
K_θ	5×10^{13}	$m_{CO_2,1}$	0	α_θ	2.5
$m_{H^+,\theta}$	− 2.5	$m_{CO_2,2}$	0.5		
$m_{CO_2,\theta}$	− 0.5	$m_{CO_2,3}$	0.5		

the interface:

$$E = \Phi_s - \Phi_l \tag{49}$$

The reversible potential is for the anodic reaction is constant at −0.440 V and for the cathodic reaction is calculated via Eq. 50 [21].

$$E_{rev,H^+} = -\frac{2.303RT_K}{F} \cdot pH_{bulk} \tag{50}$$

The Van 't Hoff equation (Eq. 51) is used to evaluate the temperature dependency of the surface kinetics by adjusting the kinetic constants k_{0,H^+}, $k_{0,1}$, and $k_{0,3}$ provided in Table 7. The activation energies used here are the updated values estimated by Kahyarian and Nešić in their 2020 paper [6].

$$k_j = k_{0,j} e^{\frac{-\Delta H_j}{R\left(T_K - T_{ref}\right)}} \tag{51}$$

Where k_j is the temperature dependent kinetic parameter of reaction j, ΔH_j is the activation energy (J) provided in Table 8, and T_{ref} is the reference temperature (283.15 K).

3.6. Boundary layer reaction kinetics

The constants calculated from the values in Table 4 are used to calculate the equilibrium conditions of the bulk fluid, however the species concentrations between the surface and the bulk are not in a state of equilibrium. The corrosion caused by the electrochemical reactions at the metal surface introduces a flux of ions which shifts the system from the bulk equilibrium. The slow rate of the CO_2 hydration reaction (Eq. 1) relative to the diffusion rate of the active species prevents the system from readily adapting to the surface flux. Due to the non-equilibrium condition in the boundary layer it is necessary to model the individual reaction kinetics to account for the boundary layer speciation.

The reactions occurring in the fluid are reversible, it is therefore possible to model the transient response of the species to the surface flux by isolating their forward and backward reaction rates. The kinetic equations for each of the reversible reactions occurring in solution are shown in Table 9, with the corresponding rate constants in Table 10.

From the kinetic equations, it is possible to derive a set of ordinary differential equations describing the rate of change of each aqueous species. These equations are used to calculate the speciation through the boundary layer based on local species concentrations and individual rates of reaction:

$$\frac{\mathrm{d}}{\mathrm{d}t}\left[CO_{2\,(aq)}\right] = -r_1 - r_5 \tag{58}$$

$$\frac{\mathrm{d}}{\mathrm{d}t}\left[H_2CO_3\right] = r_1 - r_2 \tag{59}$$

$$\frac{\mathrm{d}}{\mathrm{d}t}\left[HCO_3^-\right] = r_2 - r_3 + r_5 - r_6 \tag{60}$$

$$\frac{\mathrm{d}}{\mathrm{d}t}\left[CO_3^{2-}\right] = r_3 + r_6 \tag{61}$$

$$\frac{\mathrm{d}}{\mathrm{d}t}\left[H^+\right] = r_2 + r_3 + r_4 \tag{62}$$

Table 8
Activation energy of kinetic parameters used to calculate temperature dependency.

Kinetic Parameter	Activation Energy (J)
k_{H^+}	83,200
k_1	126,800
k_3	63,000

Table 9
Kinetics equations for reversible reactions in solution.

Reaction	Kinetics Equation	
$CO_{2_{(aq)}} + H_2O_{(l)} \rightleftharpoons H_2CO_{3_{(aq)}}$	$r_1 = k_{f,Hyd} \cdot a_{CO_2} - k_{b,Hyd} \cdot a_{H_2CO_3}$	(52)
$H_2CO_{3(aq)} \rightleftharpoons HCO^-_{3(aq)} + H^+_{(aq)}$	$r_2 = k_{f,ca} \cdot a_{H_2CO_3} - k_{b,ca} \cdot a_{HCO_3^-} \cdot a_{H^+}$	(53)
$HCO^-_{3_{(aq)}} \rightleftharpoons CO^{2-}_{3_{(aq)}} + H^+_{(aq)}$	$r_3 = k_{f,bi} \cdot a_{HCO_3^-} - k_{b,bi} \cdot a_{CO_3^{2-}} \cdot a_{H^+}$	(54)
$H_2O_{(l)} \rightleftharpoons H^+_{(aq)} + OH^-_{(aq)}$	$r_4 = k_{f,w} \cdot a_{H_2O} - k_{b,w} \cdot a_{OH^-} \cdot a_{H^+}$	(55)
$CO_{2\,(aq)} + OH^-_{(aq)} \rightleftharpoons HCO^-_{3(aq)}$	$r_5 = k_{f,hyd,OH} \cdot a_{CO_2} \cdot a_{OH^-} - k_{b,hy\text{–}H} \cdot a_{HCO_3^-}$	(56)
$HCO^-_{3(aq)} + OH^-_{(aq)} \rightleftharpoons CO_3{}^{2-}_{(aq)} + H_2O_{(l)}$	$r_6 = k_{f,bi,OH} \cdot a_{HCO_3^-} \cdot a_{OH^-} - k_{b,bi\text{–}H} \cdot a_{CO_3^{2-}} \cdot a_{H_2O}$	(57)

Table 10
Kinetic reaction rate constants for reversible reactions in solution [6].

Constant	Definition	Formula	Units
$k_{b,hyd}$	$\frac{k_{f,hyd}}{K_{Hyd}}$	$4.86 \times 10^{12} e^{-\left(\frac{64485}{RT_K}\right)}$	s^{-1}
$k_{b,ca}$	$\frac{k_{f,ca}}{K_{ca}}$	4.7×10^{10}	$M^{-1} \cdot s$
$k_{f,bi}$	$K_{bi} \cdot K_{b,bi}$	$2.03 \times 10^{7} e^{-\left(\frac{35269}{RT_K}\right)}$	s^{-1}
$k_{b,w}$	$\frac{k_{f,w}}{K_w}$	1.12×10^{11}	$M^{-1} \cdot s^{-1}$
$k_{f,hyd,OH}$	$k_{b,hyd,OH} \cdot \left(\frac{K_{ca} \cdot K_{Hyd}}{K_w}\right)$	$4.2 \times 10^{13} e^{-\left(\frac{55438}{RT_K}\right)}$	$M^{-1} \cdot s^{-1}$
$k_{f,bi,OH}$	$k_{b,bi,OH} \cdot \left(\frac{K_{bi}}{K_w}\right)$	6×10^{9}	$M^{-1} \cdot s^{-1}$

$$\frac{\mathrm{d}}{\mathrm{d}t}\left[OH^-\right] = r_4 - r_5 - r_6 \tag{63}$$

3.7. Data sweeps and storage

There are five key input parameters that influence the outputs of the model: temperature, CO_2 partial pressure, bulk pH, bulk fluid velocity, and pipe diameter. For a given combination of these inputs, a single run of the model with produce a single set of outputs. Within COMSOL Multiphysics® there is the functionality to perform parametric sweeps, calculating solutions for various values of given input parameters. LiveLink™ for MATLAB® was used to run these parametric sweeps via MATLAB to reduce solver times and allow data storage to be limited to only relevant output variables. Additionally, running the model in this way ensured that the domain was correctly recalculated and re-meshed when an input variable resulted in a change to the size of the boundary layer.

A function was generated from the COMSOL model including a single parametric sweep of P_{CO_2} as pressure does not influence the size of domain, allowing computing time to be reduced by using the previous solution as the initial value for the next set of parameters. The function code for the model was then called from a main script, into which all values of the parameters being varied were included as inputs. Via an iterative process, individual parameters were varied one at a time, with relevant output variables being extracted and stored in n-dimensional output arrays, where n is the number of parameters being assessed. Temperature and pressure were varied within the main script, running the parametric sweep of P_{CO_2} for each variable combination.

A total of 26,708 unique input conditions were initially assessed with temperature and velocity varying linearly from 273.15 to 313.15 K (0–40 °C) and 1–10 $m \cdot s^{-1}$ respectively, and partial pressure varying logarithmically from 0.1 to 10 bar across bulk pHs of 5, 5.5, 6, and 6.5 (see Table 1). The resulting log-linear data set was then used to generate contour maps of output values for each of the four bulk pH conditions. It should be noted here that for a given set of input values, the local pH through the boundary layer will vary as a function of the local H^+ activity but the temperature remains constant.

4. Results and discussion

4.1. Corrosion rate

For each set of initial conditions, the corrosion rate of the steel surface was calculated from the local anodic current density (Eqs. 45–47) and then converted from $m \cdot s^{-1}$ to the more usual form of $mm \cdot yr^{-1}$ using Eq. 64. The resultant outputs over the data range have been used to generate contour maps of corrosion rate (Fig. 4) to show the change in response to varying input conditions. Due to the results spanning multiple orders of magnitude, the common logarithm of the corrosion rate ($\log_{10}(CR)$) is shown.

$$CR\left(\frac{\mathrm{mm}}{\mathrm{yr}}\right) = CR\left(\frac{\mathrm{m}}{\mathrm{s}}\right) \times 1000 \times 365.25 \times 24 \times 60 \times 60 \tag{64}$$

At each of the bulk pH values evaluated between 5 and 6.5, a similar corrosion rate output is produced with varying temperature and partial pressure of CO_2. The highest rates of corrosion, reaching around $10\ mm \cdot yr^{-1}$ in each instance, are consistently seen in the top right corner of the contour maps (Fig. 4) where temperature and pressure are greatest. The higher rates of species transport, species dissociation and charge-transfer rates at the higher temperatures, combined with the increased availability of dissolved aqueous CO_2 species at higher pressures (Eq. 25) all act to accelerate the anodic dissolution of Fe.

At lower temperatures however, there is a clear transition to a region in which the corrosion rate starts to become independent of P_{CO2}, indicated by the near-vertical contour lines. This represents the transition from the mass-transport limited region to the charge-transfer limited region in which the cathodic current is insensitive to partial pressure, as shown experimentally by both Kahyarian and Nešić [6] and Tran et al. [10]. Under these conditions the increased availability of electroactive H^+ ions at the surface, due to the greater solubility of CO_2, becomes less significant as the speed of the electrochemical reactions becomes the rate controlling factor. The corrosion response does

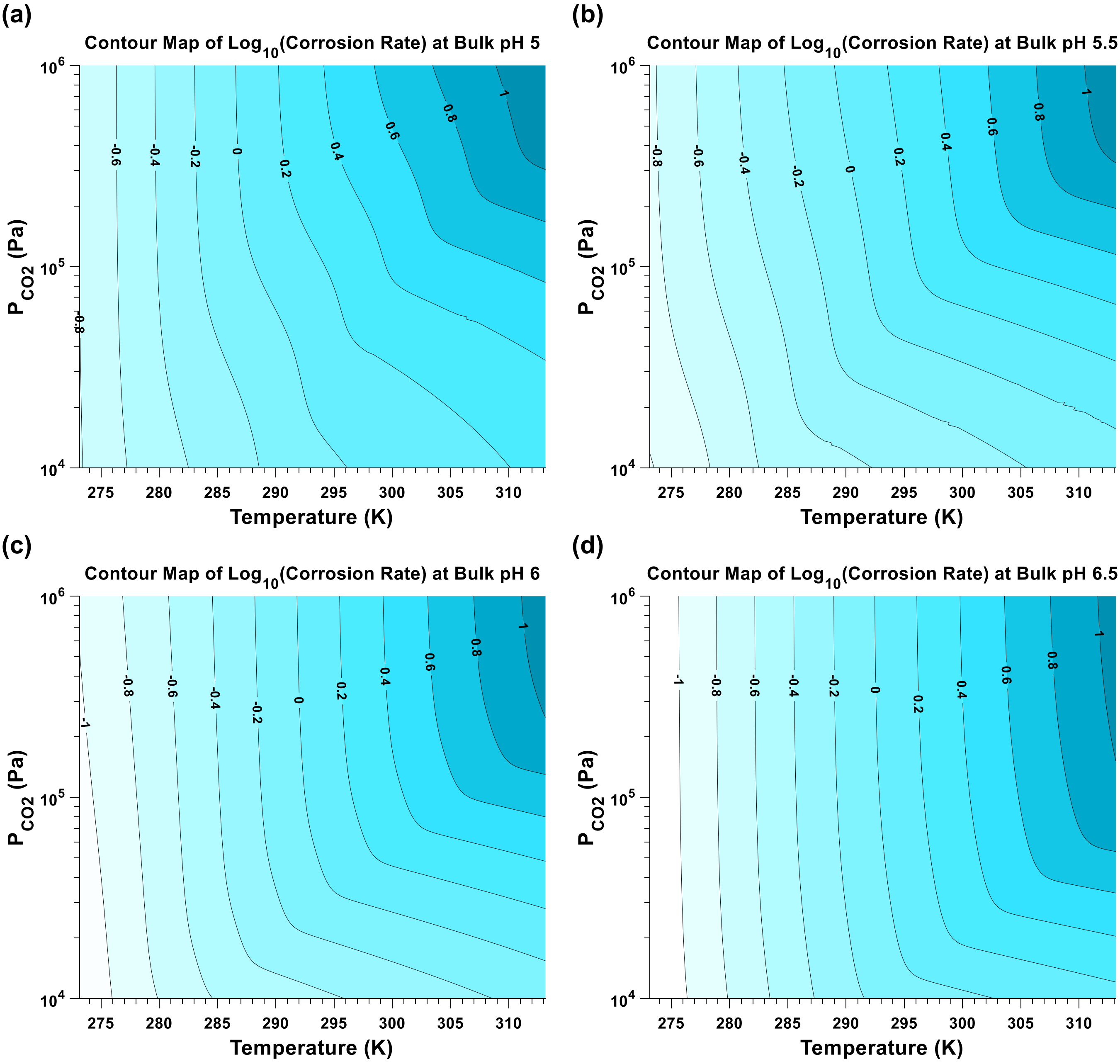

Fig. 4. Contour maps of the common logarithm of the corrosion rate ($mm \cdot yr^{-1}$) as a function of temperature and pressure at bulk pH: (a) 5 (b) 5.5 (c) 6 and (d) 6.5.

however become more sensitive to temperature in this region as higher temperatures directly increase the anodic reaction rate.

The influence of temperature on the mass-transport controlled region can be observed by evaluating the corrosion rate as a function of bulk fluid velocity, as shown in Fig. 5. While the velocity of the flow does not directly impact the fluid chemistry, higher flow rates accelerate mass transport rates due to the increased turbulence. Additionally, the boundary layer thins, reducing the distance between the surface and the bulk solution. As a result, the corrosion rate will increase with fluid velocity while the system is mass-transport limited, reaching a plateau once the system becomes charge-transfer limited.

At the highest temperature of 313.15 K (40 °C), the plateau in the corrosion rate is only seen when the bulk pH is as high as 6.5 (Fig. 5(d)), with the corrosion rate continuing to increase across the entire range of velocities for the lower pH values. This suggests that at higher temperatures the surface reactions are sufficiently fast to maintain a rate of H^+ consumption above the rate of supply. As temperature decreases, the system reaches the charge-transfer limit at progressively lower velocities as the rate of the surface reactions slow down.

The relative increase in corrosion rate as a function of velocity can also be seen to reduce as the bulk pH is increased. This effect can be seen across all temperatures, indicating that this is likely due to the reduced bulk concentration of H^+ at the higher pH. A lower bulk H^+ concentration diminishes the impact of increased mass transport rates as there are fewer ions available to be transported from the bulk to the surface.

Interestingly, an increase in the corrosion rate can be observed at bulk pH 6.5, particularly at the higher temperatures when compared to the lower pH values. Generally, it would be expected that corrosion rate decreases as pH increases due to the reduced availability of H^+ ions in the bulk solution [2,10]. However, as can be seen in Fig. 3, it is around this pH that the relative concentration of HCO_3^- starts to increase significantly. The additional HCO_3^- ions can dissociate (Eq. 3) and

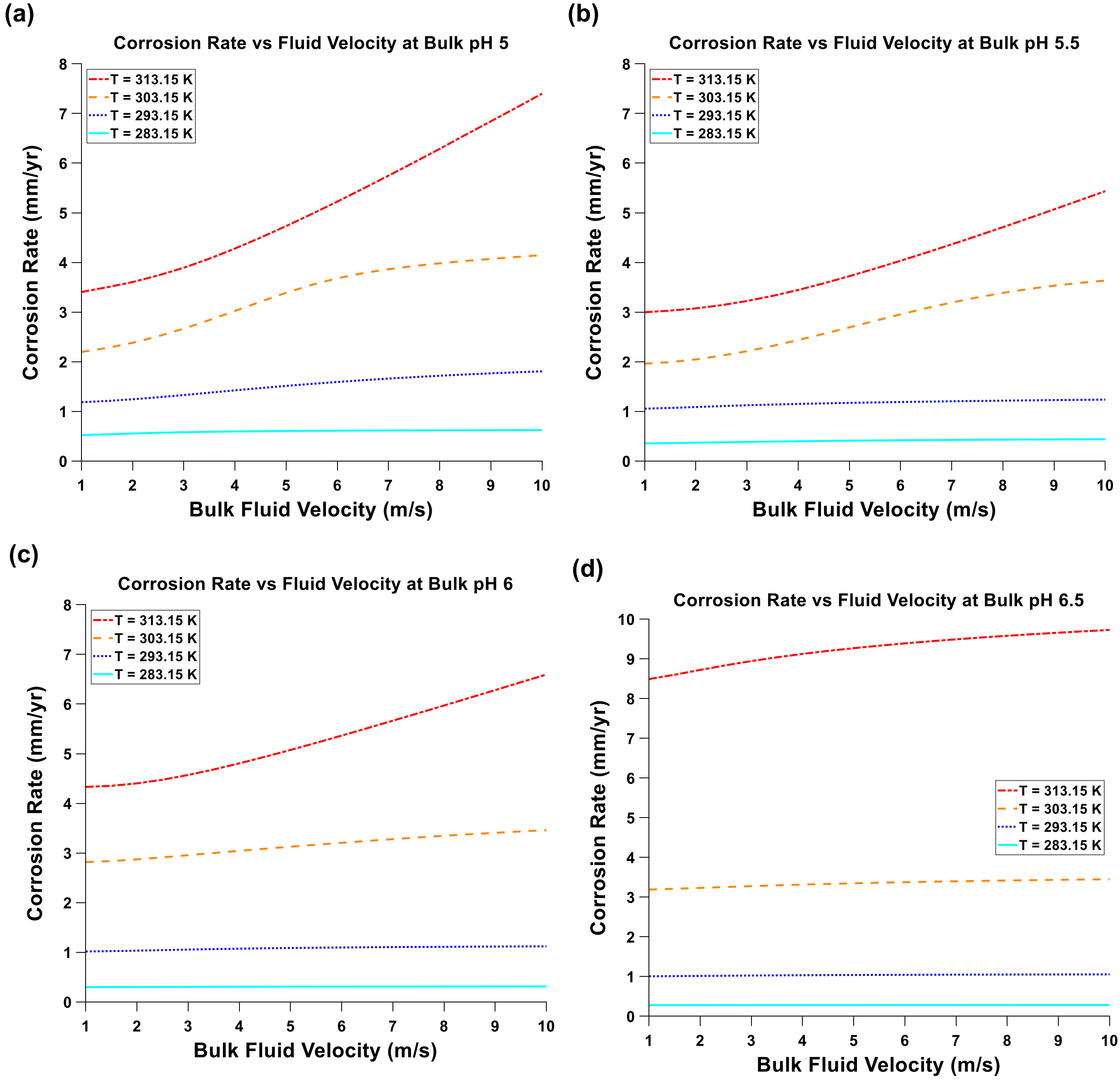

Fig. 5. Plots of corrosion rate as a function of velocity in a 0.1 m diameter pipe at 1 bar P_{CO2} at bulk pH: (a) 5 (b) 5.5 (c) 6 and (d) 6.5.

increase the production of H^+ near the surface.

A consequence of supplying H^+ via the dissociation reaction is that the local CO_3^{2-} concentration is also increased. As a result, this means that under high pH, high temperature conditions it is more likely $FeCO_3$ would begin to form a protective layer on the surface, reducing the corrosion rate [28,41,42]. However, it is important to remember that the formation of surface corrosion products and their protective properties is not considered within this model. Therefore, the increase in HCO_3^- under the higher pH conditions correlates to a higher predicted corrosion rate.

4.2. Surface pH

To determine the surface pH, the H^+ concentration was evaluated at the first node point away from the surface boundary. The pH was not evaluated directly on the surface node as the kinetic equations used to counterbalance the loss of H^+ ions in the surface reactions are not applied to the boundary. This leads to artificially inflated values for the surface pH.

$$pH_{surface} = -\log_{10}\left(a_{H^+ surface}\right) \tag{65}$$

Where $a_{H^+ surface}$ is the hydrogen ion activity (M) at the surface.

Fig. 6 displays the change in surface pH as a function of temperature and P_{CO2} at the various bulk pH values.

Across all the bulk pH conditions evaluated, a similar response was seen in the surface pH, with the surface pH being universally higher due to the consumption of H^+ ions as part of the cathodic reaction.

Notable differences between the surface and bulk pH values are observed in each of the plots shown in Fig. 6, with the pH increasing by almost 2 units in some cases. While it is difficult to isolate the individual contributions of the various reactions and transport terms to the local H^+ concentration, the H_2CO_3 buffering mechanism likely plays a significant role. In a separate study comparing this model against the direct

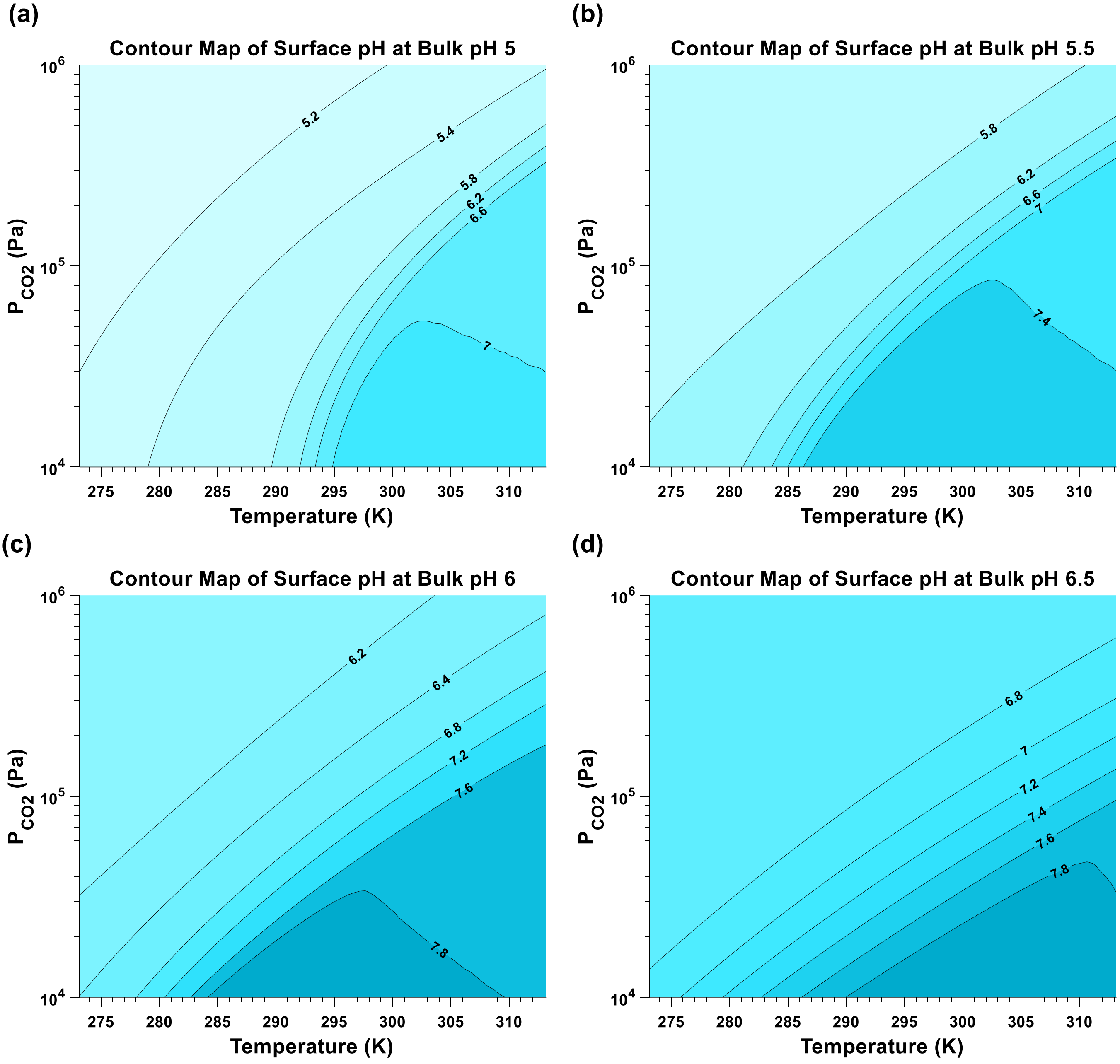

Fig. 6. Contour maps of the surface pH as a function of temperature and pressure at bulk pH: (a) 5 (b) 5.5 (c) 6 and (d) 6.5.

reduction model by Nordsveen et al. [21], it was found that the direct reduction model saw a maximum pH increase of just 0.5 units across the same range of conditions [43]. When there is a secondary H_2CO_3 reduction reaction supplying H^+ at the surface, this acts as an immediate counter-balance to the depletion of H^+ ions. The buffering mechanism employed here supplies H^+ through dissociation in solution, but not necessarily at the surface. The consequence of this is that, although the lost H^+ ions are replenished within the boundary layer, the concentration immediately adjacent to the surface is lower, resulting a higher predicted pH at this point.

Under high pressure, low temperature conditions the surface pH converged towards the bulk pH value as the high concentration of H_2CO_3 and low surface reaction rates allow for rapid replenishment of consumed ions through dissociation. The result of this is a charge-transfer limited system which does not result in significant depletion of H^+ ions close to the surface.

As the temperature is increased and the pressure is lowered, the system shifts towards mass-transport control, with ions being consumed almost immediately after reaching the surface, resulting in very high surface pH values relative to the bulk. Within this mass-transport controlled region, there is a clear transition point within each contour map at which surface pH begins to decrease with temperature.

From Fig. 4, it is known that the corrosion rate, and therefore the rate of the cathodic reaction (Eq. 8), becomes less sensitive to temperature once the system is no longer charge-transfer controlled. Consequently, the relative rate of consumption of H^+ ions with increasing temperature is reduced in the mass-transport controlled region.

On the other hand, the rate of supply of H^+ continues to increase with temperature due to increasing rates of dissociation and greater species transport from the bulk to the surface. This is supported by the higher surface pH causing a shift in the equilibrium state towards CO_3^{2-} production (Fig. 3), resulting in rapid dissociation of the highly concentrated HCO_3^- ions (Eq. 3) and the production of additional H^+ ions.

With the relative rate of H^+ consumption being reduced and the

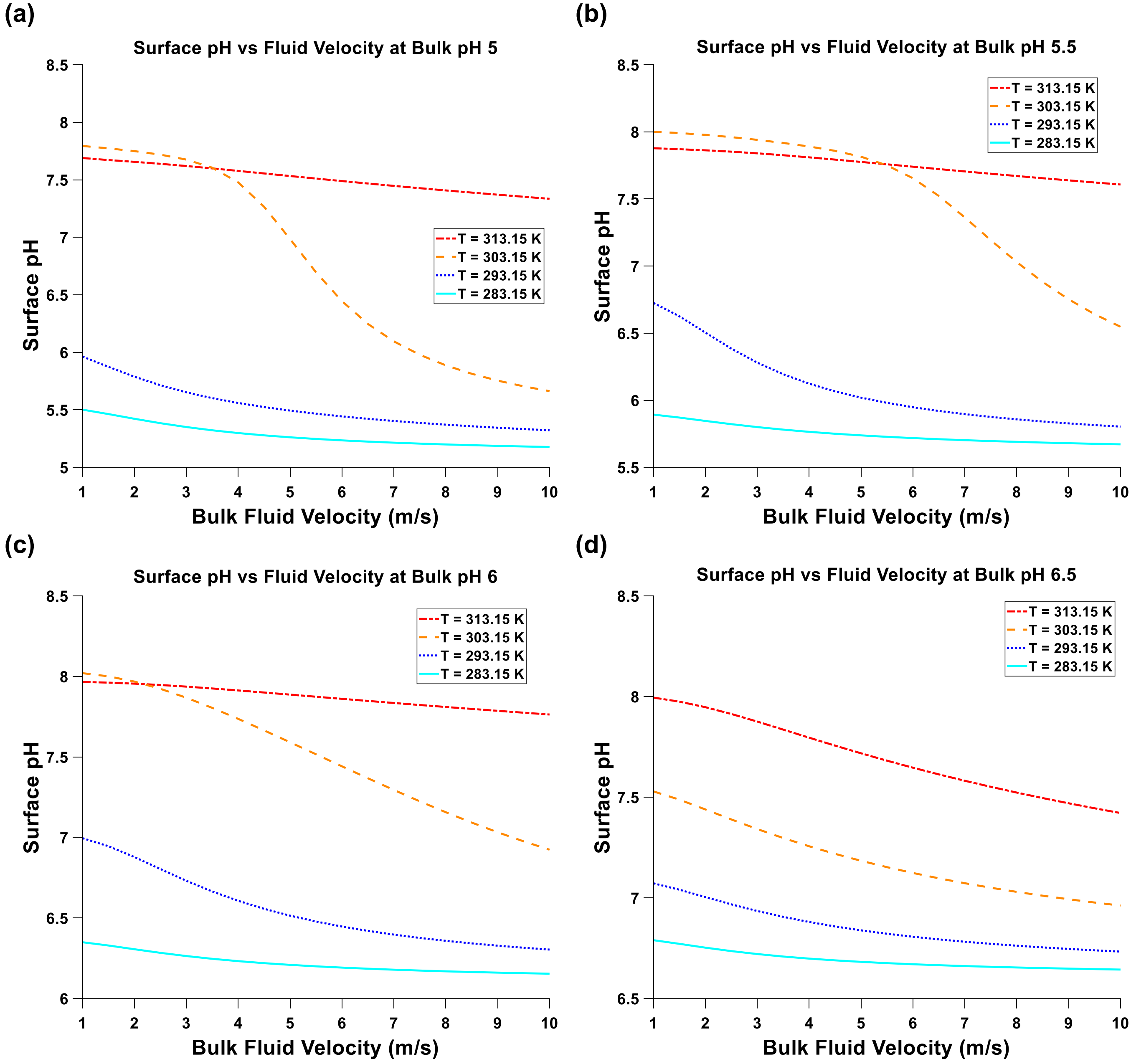

Fig. 7. Plots of surface pH as a function of velocity in a 0.1 m diameter pipe at 1 bar P_{CO2} at bulk pH: (a) 5 (b) 5.5 (c) 6 and (d) 6.5.

increasing production rate, an inverse relationship between temperature and surface pH can be observed in the high temperature, low pressure region.

The response of the surface pH to change in bulk velocity is shown in Fig. 7 and once again two trends can be identified depending on the current limiting mechanism. Under mass-transport controlled conditions the surface pH tends towards the bulk pH values as fluid velocity is increased.

The higher flow velocities reduce the height of the boundary layer resulting in steeper concentrations gradients while simultaneously inducing greater turbulence within the flow. Together this raises both the molecular and turbulent diffusion, increasing species transport between the surface and the bulk. As a result, when the surface reactions reach their limiting current, the increase in the supply of ions to the surface acts to reduce the deviation from the bulk pH. This effect is not seen however in the mass-transport controlled region however, as shown by the 313.15 K lines at pHs 5, 5.5 and 6 where the surface pH remains high due to the surface reactions also being accelerated by the increased rate of supply. A small reduction in surface pH is observed due to the substantial increase in mass transport rates, however the response is linear, as opposed to the exponential decay produced in the charge-transfer regions. In some cases, the transition between the two regimes can be identified by a sudden change in the surface pH, as is the case at 303.15 K in Fig. 7(a), seen at around 4 m·s^{-1}.

4.3. Saturation index

The saturation index (SI) is a measure of the degree of supersaturation of $FeCO_3$ within a system and so can be used to predict when precipitation is likely to occur. A saturation index of zero represents the point at which a solution becomes supersaturated, and precipitation becomes thermodynamically favoured. As the $FeCO_3$ saturation increases beyond this point, precipitation becomes more thermodynamically stable and the rate of nucleation and growth accelerates [28,42].

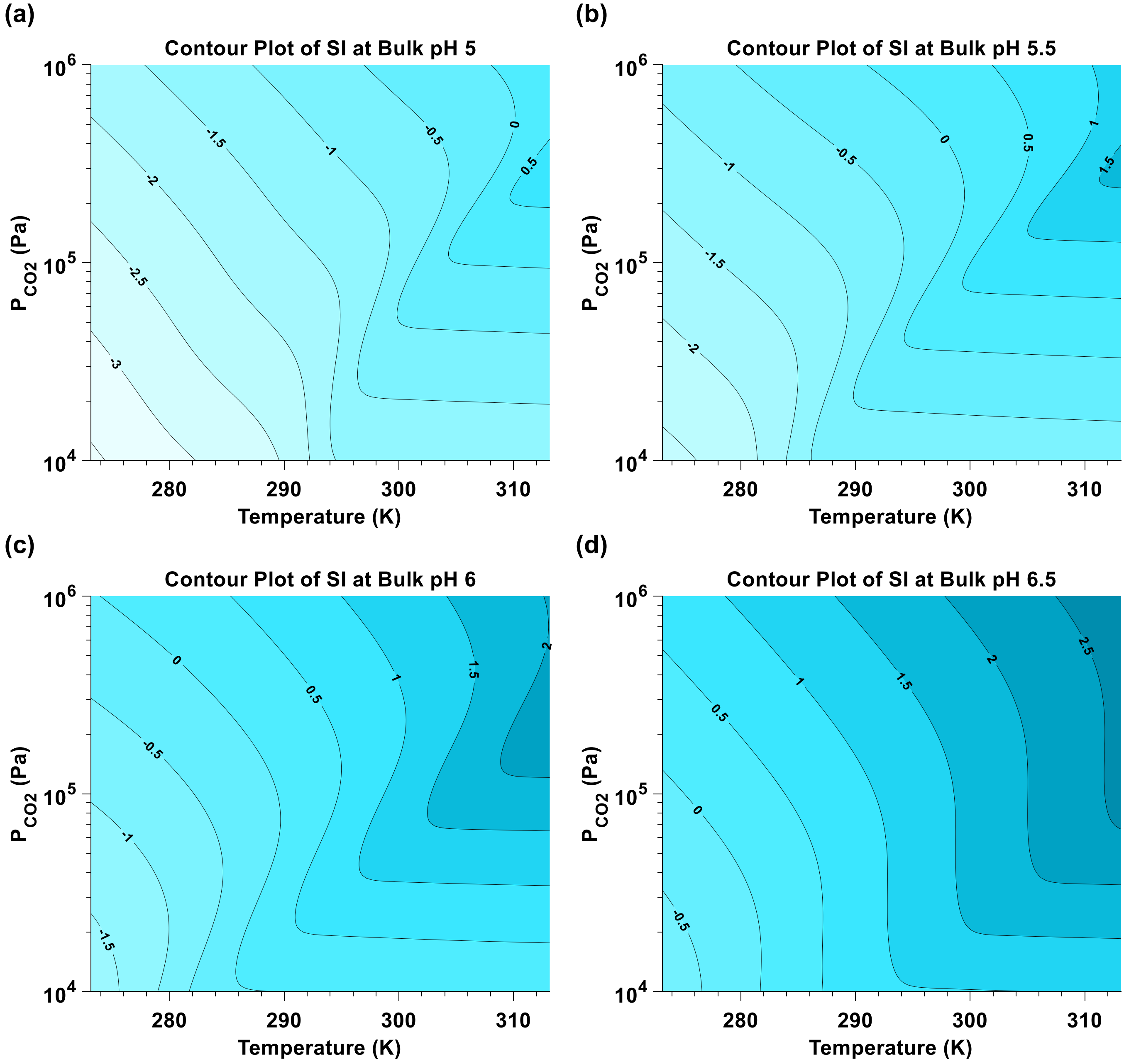

Fig. 8. Contour maps of surface saturation index of $FeCO_3$ as a function of velocity for a 0.1 m diameter pipe at 1 bar P_{CO2} at bulk pH: (a) 5 (b) 5.5 (c) 6 and (d) 6.5.

The saturation index is a function of the saturation ratio, which is a calculated from the local activities of Fe^{2+} and CO_3^{2-}.

$$SI = \log_{10}(SR) \tag{66}$$

$$SR = \frac{a_{Fe^{2+}} \cdot a_{CO_3{}^{2-}}}{K_{sp}} \tag{67}$$

Where SR is the saturation ratio, $a_{Fe^{2+}}$ and $a_{CO_3^{2-}}$ are the respective species activities (M), and K_{sp} is the solubility limit (M^2). For the purposes of this work, the solubility limit formula proposed by Greenberg and Tomson [44] (Eq. 68) has been used.

$$\log_{10}(K_{sp}) = -59.2385 - 0.041377T_K - \frac{2.1963}{T_K} + 24.5724\log_{10}(T_K) \tag{68}$$

The contour maps of the surface SI shown in Fig. 8 clearly demonstrate two different response patterns depending on whether the surface reactions are charger-transfer limited or mass-transport limited.

Under both regimes there is a consistent increase in SI with pressure, as the increased concentration of H_2CO_3 consequently raises the CO_3^{2-} concentration in both the bulk and at the surface. As the dissolution of CO_2 occurs independently of the electrochemical surface reactions, the higher partial pressure acts to raise the SI regardless of the limiting mechanism. Therefore, in regions where the behaviour is stable, a consistent increase in SI is seen in response to increasing pressures, which is primarily due to change in the CO_3^{2-} concentration.

Conversely, the local Fe^{2+} concentration closely follows the corrosion rate response (Fig. 4) due to the anodic reaction resulting in the dissolution of Fe from the surface into solution. As the corrosion rate becomes less sensitive to temperature when under mass-transport control, the saturation index also begins to plateau in this region. The production of CO_3^{2-} at the surface does increase with temperature due to the higher pH, however the corresponding increase in the species transport rates acts to move these ions away from the surface more rapidly. The overall effect is relatively stable surface SI for any given pressure, an effect which is not seen in the charge-transfer controlled region due to the strong dependence of iron dissolution on temperature.

In the transition between the two regions, a much more complex response is produced due to the competing interactions affecting both Fe^{2+} and CO_3^{2-}. The difficulty in accurately predicting the $FeCO_3$ saturation response is highlighted in this region, with the shapes of the contours varying significantly depending on the conditions.

The influence of the bulk pH on the SI, however, is much more consistent. As bulk pH is increased from 5 (Fig. 8(a)) to 6.5 (Fig. 8(d)) a steady increase in $FeCO_3$ saturation can be observed, with the surface being supersaturated ($SI > 0$) across almost all conditions at the highest pH. Once again, this can be explained via the shift in the equilibrium state from H_2CO_3 dominated towards CO_3^{2-} dominated (Fig. 3). The significant rise in the concentration of CO_3^{2-} ions in the bulk solution is sufficient to determine the behaviour of the SI in response to pH, irrespective of the changes to the surface electrochemistry.

It is important to remember that although these values provide an indication of the likelihood of $FeCO_3$ precipitation, the formation of protective films is not modelled here. Therefore, under higher pH conditions, when the SI is significantly above 0, the accuracy of the model needs to be considered. As discussed previously, it is known that current corrosion models become less representative of the real-world scenarios as corrosion products begin to form due to their interference with the corrosion processes. Previous works have shown a direct correlation between the degree of supersaturation and the rate of growth of these corrosion products, implying diminishing confidence in the model outputs as the predicted SI continues to increase [28,45]. However, from the plots shown in Fig. 8, it is possible to gauge the conditions under which protective films may start to form and impact the accuracy of the model. Reliably accounting for the formation, growth, and influence of $FeCO_3$ films under these conditions represents a clear next step in the development of this comprehensive mechanistic corrosion model.

5. Conclusion

The output response of a comprehensive mechanistic model of CO_2 corrosion has been evaluated across thousands of combinations of input conditions for temperature, partial pressure of CO_2, velocity, and bulk pH. Two distinct response patterns have been identified dependent upon the limiting behaviour of the system.

Under low temperature, high pressure conditions, the model predicts an output that is charge-transfer limited. As the bulk pH is increased from 5 to 6.5, the size of this charge-transfer limited region was extended to higher temperatures. Under these conditions, changes to the partial pressure of CO_2 had minimal impact on the corrosion rate and the surface pH did not deviate far from the bulk value. However, the corrosion rate and the surface $FeCO_3$ saturation index were highly sensitive to changes in temperature due to the associated increase in the anodic iron dissolution reaction.

At higher temperatures and lower pressures, the limiting behaviour transitioned to mass-transport control, with H^+ ions being consumed rapidly upon reaching the surface. Under the mass-transport limited regime, the predicted corrosion rates became much more sensitive to changes in pressure with the surface pH rising significantly above that of the bulk pH. Both corrosion rate and $FeCO_3$ saturation were less impacted by temperature changes in this region due to supply of H^+ ions to the surface limiting the rates of the surface reactions. Instead, the behaviour was found to be primarily determined by changes to the rates of species transport through the boundary layer, therefore becoming more sensitive to hydrodynamic changes.

Limits of the model were identified at higher pH conditions due to a significant increase in the local SI at the surface, particularly at higher temperatures and higher pressures. The formation of protective corrosion products under these conditions was found to be highly likely, reducing the accuracy of the corrosion model. Research surrounding the fundamental understanding of the precipitation kinetics being undertaken at the University of Leeds is intended to improve the model in this regard through further study.

CRediT authorship contribution statement

Mariana C. Folena: Writing – review & editing, Supervision. **Gregory de Boer:** Writing – review & editing, Supervision, Methodology, Formal analysis. **Richard C. Woollam:** Writing – review & editing, Supervision, Methodology, Formal analysis. **Michael Jones:** Writing – review & editing, Writing – original draft, Validation, Software, Methodology, Investigation, Formal analysis, Data curation. **Joshua Owen:** Writing – review & editing, Supervision, Methodology, Formal analysis. **Hanan Farhat:** Writing – review & editing, Supervision. **Richard Barker:** Writing – review & editing, Supervision, Resources, Project administration, Methodology, Funding acquisition, Formal analysis, Conceptualization.

Declaration of Competing Interest

The authors declare that they have no known competing financial interests or personal relationships that could have appeared to influence the work reported in this paper.

Data availability

The raw/processed data required to reproduce these findings cannot be shared at this time as the data also forms part of an ongoing study.

References

[1] A. Kahyarian, M. Singer, S. Nešić, Modeling of uniform CO_2 corrosion of mild steel in gas transportation systems: a review, J. Nat. Gas Sci. Eng. 29 (2016) 530–549, https://doi.org/10.1016/j.jngse.2015.12.052.

[2] S. Nešić, Key issues related to modelling of internal corrosion of oil and gas pipelines – a review, Corros. Sci. 49 (2007) 4308–4338, https://doi.org/10.1016/j.corsci.2007.06.006.

[3] R.C. Woollam, S.E. Hernandez, 2006. Assessment and Comparison of CO_2 Corrosion Prediction Models, SPE International, SPE 100673.

[4] R. Nyborg, 2002. Overview of CO_2 Corrosion Models for Wells and Pipelines, NACE International. 02233.

[5] R. Nyborg, CO_2 Corrosion Models for Oil and Gas Production Systems, NACE International, 2010, p. 10371.

[6] A. Kahyarian, S. Nešić, On the mechanism of carbon dioxide corrosion of mild steel: experimental investigation and mathematical modeling at elevated pressures and non-ideal solutions, Corros. Sci. 173 (2020) 1–27, https://doi.org/10.1016/j.corsci.2020.108719.

[7] A. Kahyarian, S. Nešić, A new narrative for CO_2 corrosion of mild steel, J. Electrochem. Soc. 166 (2019) C3048–C3063, https://doi.org/10.1149/2.0071911jes.

[8] C. de Waard, D.E. Milliams, Carbonic acid corrosion of steel, Corrosion 31 (1975) 177–181, https://doi.org/10.5006/0010-9312-31.5.177.

[9] E. Remita, B. Tribollet, E. Sutter, V. Vivier, F. Ropital, J. Kittel, Hydrogen evolution in aqueous solutions containing dissolved CO_2: quantitative contribution of the buffering effect, Corros. Sci. 50 (2008) 1433–1440, https://doi.org/10.1016/j.corsci.2007.12.007.

[10] T. Tran, B. Brown, S. Nešić, Corrosion of Mild Steel in an Aqueous CO_2 Environment – Basic Electrochemical Mechanisms Revisited, NACE International, 2015, p. 5671.

[11] B.R. Linter, G.T. Burstein, Reactions of pipeline steels in carbon dioxide solutions, Corros. Sci. 41 (1999) 117–139, https://doi.org/10.1016/S0010-938X(98)00104-8.

[12] M.M. Alsalem, M.P. Ryan, A.N. Campbell, K.S. Campbell, Modelling of CO_2 corrosion and $FeCO_3$ formation in NaCl solutions, Chem. Eng. J. 451 (2022) 1–19, https://doi.org/10.1016/j.cej.2022.138966.

[13] U. Thorat, M. Jones, R. Woollam, J. Owen, R. Barker, H. Thompson, G. de Boer, Computational fluid dynamics driven mass transfer model for the prediction of CO_2 corrosion in pipelines, J. Pipeline Sci. Eng. (2023), https://doi.org/10.1016/j.jpse.2023.100148.

[14] J. Owen, J. Godfrey, W. Ma, G. de Boer, M. Al-Khateeb, H. Thompson, A. Neville, C. Ramsey, R. Barker, An experimental and numerical investigation of CO_2 Corrosion in a rapid expansion pipe geometry, Corros. Sci. 165 (2020), https://doi.org/10.1016/j.corsci.2019.108362.

[15] J.T. Davies. Turbulence Phenomena, first ed., Academic Press, Inc, New York, U.S.A., 1972.

[16] S. Aravinth, Prediction of heat and mass transfer for fully developed turbulent fluid flow through tubes, Int. J. Heat. Mass Transf. 43 (2000) 1399–1408, https://doi.org/10.1016/S0017-9310(99)00218-5.

[17] L.I. Stephens, J. Mauzeroll, Demystifying mathematical modeling of electrochemical systems, J. Chem. Educ. 96 (2019) 2217–2224, https://doi.org/10.1021/acs.jchemed.9b00542.

[18] D. Britz, J. Strutwolf. Digital Simulation in Electrochemistry, fourth ed., Springer International Publishing, Switzerland, 2016.

[19] S. Turgoose, R.A. Cottis, K. Lawson, Modeling of electrode processes and surface chemistry in carbon dioxide containing solutions, in: R.S. Munn (Ed.), Computer Modeling in Corrosion, Philadelphia, 1992, pp. 67–81.

[20] S. Nešić, R. Nyborg, A. Stangeland, M. Nordsveen, Mechanistic Modeling for CO_2 Corrosion with Protective Iron Carbonate Films, 01040, NACE International, 2001.

[21] M. Nordsveen, S. Nešić, R. Nyborg, A. Stangeland, A mechanistic model for carbon dioxide corrosion of mild steel in the presence of protective iron carbonate films - part 1: theory and verification, Corrosion 59 (2003) 443–456, https://doi.org/10.5006/1.3277576.

[22] S. Prabhakara, M.D. Deshpande, The no-slip boundary condition in fluid mechanics: 1. The Riddle of Fluid Sticking to the Wall in Flow, Resonance 9 (2004) 50–60, https://doi.org/10.1007/BF02834856.

[23] K.C. Misra. Introduction to Geochemistry: Principles and Applications, first ed., Wiley-Blackwell, Oxford, 2011.

[24] F.M. Song, D.W. Kirk, J.W. Graydon, D.E. Cormack, Predicting carbon dioxide corrosion of bare steel under an aqueous boundary layer, Corrosion 60 (2004) 736–748, https://doi.org/10.5006/1.3287853.

[25] S. Nešić, M. Nordsveen, R. Nyborg, A. Stangeland, A mechanistic model for carbon dioxide corrosion of mild steel in the presence of protective iron carbonate films - part 2: a numerical experiment, Corrosion 59 (2003) 489–497, https://doi.org/10.5006/1.3277579.

[26] S. Nešić, K.L.J. Lee, A mechanistic model for carbon dioxide corrosion of mild steel in the presence of protective iron carbonate films - part 3: film growth model, Corrosion 59 (2003) 616–628, https://doi.org/10.5006/1.3277592.

[27] Z. Ma, Y. Yang, B. Brown, S. Nešić, M. Singer, Investigation of precipitation kinetics of $FeCO_3$ by EQCM, Corros. Sci. 141 (2018) 195–202, https://doi.org/10.1016/j.corsci.2018.06.017.

[28] R. Barker, D. Burkle, T. Charpentier, H. Thompson, A. Neville, A review of iron carbonate ($FeCO_3$) formation in the oil and gas industry, Corros. Sci. 142 (2018) 312–341, https://doi.org/10.1016/j.corsci.2018.07.021.

[29] E. Van Hunnik, B.F.M. Pots, E.L.J.A. Hendriksen, The formation of protective $FeCO_3$ corrosion product layers in CO_2 corrosion, NACE Int. 6 (1996).

[30] D.S.K. Ting, Wall Turbulence, first ed., Academic Press, London (2016).

[31] D.B. Spalding, A single formula for the "Law of the Wall", J. Appl. Mech. 28 (1961) 455–458, https://doi.org/10.1115/1.3641728.

[32] P.K. Swamee, K.J. Akalank, Explicit equations for pipe-flow problems, J. Hydraul. Div. 102 (1976) 657–665, https://doi.org/10.1061/JYCEAJ.0004542.

[33] R.H. Notter, C.A. Sleicher, The Eddy diffusivity in the turbulent boundary layer near a wall, Chem. Eng. Sci. 26 (1971) 161–171, https://doi.org/10.1016/0009-2509(71)86088-8.

[34] S.W. Churchill, A critique of predictive and correlative models for turbulent flow and convection, Ind. Eng. Chem. Res. 35 (1996) 3122–3140, https://doi.org/10.1021/ie960012m.

[35] D.G. Archer, P. Wang, The dielectric constant of water and Debye-HückeL Limiting Law Slopes, J. Phys. Chem. Ref. Data 19 (1990) 371–411, https://doi.org/10.1063/1.555853.

[36] D. Li, Z. Duan, The speciation equilibrium coupling with phase equilibrium in the H_2O–CO_2–NaCl system From 0 to 250 °C, from 0 to 1000 bar, and from 0 to 5 molality of NaCl, Chem. Geol. 244 (2007) 730–751, https://doi.org/10.1016/j.chemgeo.2007.07.023.

[37] Z. Duan, D. Li, Coupled phase and aqueous species equilibrium of the H_2O–CO_2–NaCl–$CaCO_3$ system from 0 to 250°C, 1 to 1000 bar with NaCl concentrations up to saturation of Jalite, Geochim. Et. Cosmochim. Acta 72 (2008) 5128–5145, https://doi.org/10.1016/j.gca.2008.07.025.

[38] W.L. Marshall, E.U. Franck, Ion product of water substance, 0–1000 °C, 1–10,000 bars new international formulation and its background, J. Phys. Chem. Ref. Data 10 (1981) 295–304, https://doi.org/10.1063/1.555643.

[39] Battelle Memorial Institute, Steel – Physical and typical mechanical properties, in: Battelle Memorial Institute (Ed.), Metallic Materials Properties Development and Standardization (MMPDS), Ohio, 2017, 1-12.

[40] COMSOL. Electrodeposition Module User's Guide, sixth ed., COMSOL, Stockholm, Sweden, 2022.

[41] F. Pessu, R. Barker, A. Neville, The influence of pH on localized corrosion behavior of X65 carbon steel in CO_2-saturated brines, Corrosion 71 (2015) 1452–1466, https://doi.org/10.5006/1770.

[42] A. Dugstad, Fundamental Aspects of CO_2 Metal Loss Corrosion - Part 1: Mechanism, 06111, NACE International, 2006.

[43] M. Jones, G. de Boer, R. Woollam, J. Owen, M.C. Folena, H. Farhat, R. Barker, Assessing comprehensive mechanistic CO_2 corrosion modeling methods and their impact on predicted corrosion behavior, AMPP (2024) C2024–C20656.

[44] J. Greenberg, M. Tomson, Precipitation and dissolution kinetics and equilibria of aqueous ferrous carbonate vs temperature, Appl. Geochem. 7 (1992) 185–190, https://doi.org/10.1016/0883-2927(92)90036-3.

[45] C.Z. Jiang, N.J. Tosca, Growth kinetics of siderite at 298.15 K and 1 bar, Geochim. Et. Cosmochim. Acta 274 (2020) 97–117, https://doi.org/10.1016/j.gca.2020.01.047.